Article

Using SF$_6$ Decomposed Component Analysis for the Diagnosis of Partial Discharge Severity Initiated by Free Metal Particle Defect

Ju Tang [1], Xu Yang [1] , Dong Yang [1], Qiang Yao [2], Yulong Miao [2], Chaohai Zhang [3] and Fuping Zeng [1,*]

[1] School of Electrical Engineering, Wuhan University, Wuhan 430072, China; whtangju@whu.edu.cn (J.T.); 15102738342@126.com (X.Y.); scyangdong@163.com (D.Y.)
[2] Chongqing Electric Power Research Institute, Chongqing Power Company, Chongqing 401123, China; 2012202070085@whu.edu.cn (Q.Y.); ygxflyhigh@163.com (Y.M.)
[3] State Grid Electric Power Research Institute, Wuhan NARI Co., Ltd., Wuhan 430072, China; Yx844072450@gmail.com
* Correspondence: Fuping.Zeng@whu.edu.cn; Tel.: +86-027-6877-2323

Abstract: The decomposition characteristics of a SF$_6$ gas-insulated medium were used to diagnose the partial discharge (PD) severity in DC gas-insulated equipment (DC-GIE). First, the PD characteristics of the whole process were studied from the initial PD to the breakdown initiated by a free metal particle defect. The average discharge magnitude in a second was used to characterize the PD severity and the PD was divided into three levels: mild PD, medium PD, and dangerous PD. Second, two kinds of voltage in each of the above PD levels were selected for the decomposition experiments of SF$_6$. Results show that the negative DC-PD in these six experiments decomposes the SF$_6$ gas and generates five stable decomposed components, namely, CF$_4$, CO$_2$, SO$_2$F$_2$, SOF$_2$, and SO$_2$. The concentrations and concentration ratios of the SF$_6$ decomposed components can be associated with the PD severity. A minimum-redundancy-maximum-relevance (mRMR)-based feature selection algorithm was used to sort the concentrations and concentration ratios of the SF$_6$ decomposed components. Back propagation neural network (BPNN) and support vector machine (SVM) algorithms were used to diagnose the PD severity. The use of $C(CO_2)/CT_1$, $C(CF_4)/C(SO_2)$, $C(CO_2)/C(SOF_2)$, and $C(CF_4)/C(CO_2)$ shows good performance in diagnosing PD severity. This finding serves as a foundation in using the SF$_6$ decomposed component analysis (DCA) method to diagnose the insulation faults in DC-GIE and assess its insulation status.

Keywords: SF$_6$; partial discharge severity; DC gas-insulated equipment; feature selection; back propagation neural network; support vector machine; decomposed component analysis

---

1. Introduction

SF$_6$ possesses excellent insulating and arc-extinguishing performance and is widely used as a medium in gas-insulated equipment (GIE) because of its ability to greatly reduce the equipment size and improve system reliability [1–5]. DC-GIE received much attention due to the rapid development of high-voltage DC (HVDC) transmission and flexible HVDC technologies [6–11]. However, when partial discharge (PD) occurs inside the equipment, this phenomenon can decompose SF$_6$ and generate a series of low-fluorine sulfides (such as SF$_5$, SF$_4$, SF$_3$, and SF$_2$). These low-fluorine sulfides then react with the trace moisture and oxygen that inevitably exist in the equipment, thus generating some stable decomposition products, such as SO$_2$F$_2$, SOF$_2$, SO$_2$, CF$_4$, CO$_2$, HF, and H$_2$S and resulting in the insulation performance degradation of SF$_6$ [12–17]. Using SF$_6$ decomposed component analysis (DCA)

to diagnose the insulation faults in DC-GIE and assess its insulation status can effectively avoid the complex electromagnetic interference in the substation; this method has recently become a popular topic for researchers around the world [18–21].

The decomposition characteristics of SF_6 under four typical PD types in GIE were studied based on the DCA method [22–25], and the three-ratio method, which was similar to oil chromatographic analysis, was proposed for the recognition of the PD type. In addition to determining the discharge type, the discharge severity should be defined when assessing the insulation status of GIE. Parameters, such as apparent discharge magnitude, discharge repetition rate, and discharge time interval measured by pulse current method (PCM) are important features that characterize the discharge severity under DC conditions. However, PCM cannot be used to diagnose discharge severity in the field due to the multi-point grounding of real GIE. A large number of studies [22–27] reported the close relationships between the decomposition characteristics of the SF_6 gas-insulated medium and the type, energy consumption, and development trend of PD in GIE. Therefore, the SF_6 DCA method can be used to diagnose the PD severity in DC-GIE; however, no relevant study has been conducted about this topic.

This research develops a ball-bowl electrode to simulate the free metal particle insulation defect in DC-GIE and studies the PD characteristics of the whole process from the initial PD to the breakdown by using the built experimental platform. Based on the PD characteristics, the PD initiated by free metal particles is divided into three levels: mild PD, medium PD, and dangerous PD. Two kinds of voltage in each of the above PD levels are selected for the decomposition experiments of SF_6, and the decomposed components are measured by gas chromatography/mass spectrometry (GC/MS). A minimum-redundancy-maximum-relevance (mRMR)-based feature selection algorithm [28–33] is used to sort the concentrations and concentration ratios of SF_6 decomposed components. Back propagation neural network (BPNN) [24,34–41] and support vector machine (SVM) [41–47] algorithms are used to diagnose the PD severity. This research proposes the feature subset that can effectively characterize the PD severity and serves as a foundation for using the DCA method to diagnose the insulation faults in DC-GIE and assess its insulation status.

2. Experiment

2.1. Experimental Platform

The experimental platform of SF_6 decomposition under negative DC-PD is shown in Figure 1, which mainly includes four parts: the HVDC supply system, PD gas chamber, decomposed component detection system, and PD signal detection system.
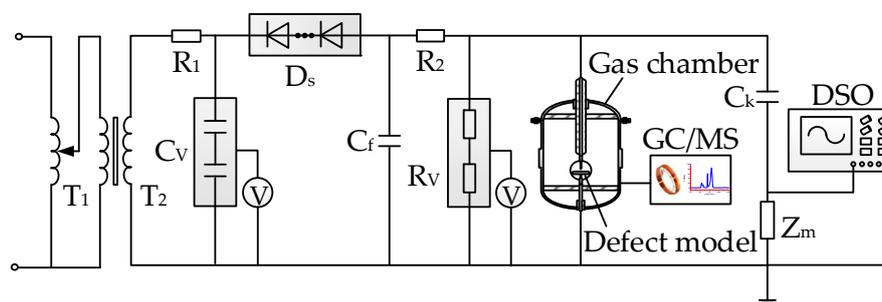
Figure 1. Experimental platform of SF_6 decomposition under negative DC-partial discharge (PD).

The HVDC supply system mainly includes: voltage regulator (T_1: 0–380 V), testing transformer (T_2: 50 kVA/100 kV), HV silicon stack (D_s: 100 kV/5 A), filter capacitor (C_f: 0.2 μF), protective resistor (R_1: 20 kΩ, R_2: 20 kΩ), capacitive voltage divider (C_v, capacitance of HV arm: 500 pF, capacitance of low-voltage (LV) arm: 0.5 μF), and resistive voltage divider (R_v, resistance of HV arm: 220 MΩ, resistance of LV arm: 22 kΩ).

The PD gas chamber is made of stainless steel, has volume of 60 L that can withstand 0.7 MPa gas pressure, and has a good sealing performance as shown in Figure 2.

The decomposed component detection system uses the GC/MS (Shimadzu QP-2010Ultra, precision: 0.01 ppm, accuracy: ±10%, Shimadzu, Kyoto, Japan) to quantitatively measure the sample gas. The working conditions of GC/MS are as follows: injection port temperature: 220 °C; sample volume: 1 mL; total flow: 16.2 mL/min; pillar flow: 1.20 mL/min; linear velocity: 28.0 cm/s; blow flow: 3.0 mL/min; split ratio 10:1; connecter temperature: 220 °C; ion source: 200 °C; and ionization pattern: electron impact. The external standard method is used for the quantitative indication of SF_6 decomposed components [22]. The retention time and absolute calibration factor K_i of CF_4, CO_2, SO_2F_2, SOF_2, and SO_2 are shown in Table 1.
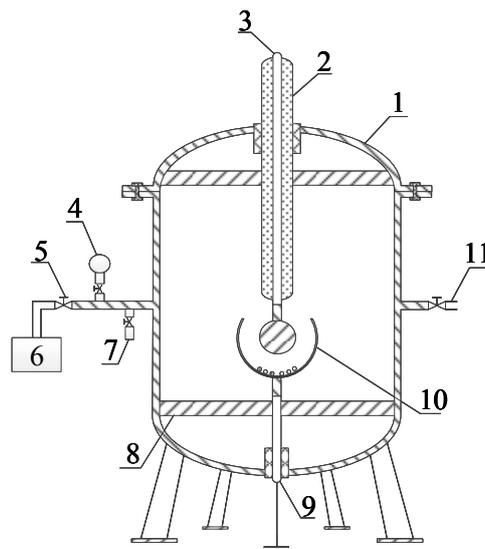

Figure 2. Structure of PD gas chamber: 1: gas chamber; 2: High-voltage (HV) bushing; 3: HV conductor; 4: ball valve; 5: vacuum pressure gauge; 6: vacuum pump; 7: injection port; 8: support insulator; 9: ground conductor; 10: insulation defect; and 11: sampling port.

Table 1. The retention time and absolute calibration factor K_i.

Decomposed Components	Retention Time/s	$K_i/10^{-5}$	R^2
CF_4	4.320	2.838	0.999
CO_2	4.815	2.525	0.999
SO_2F_2	5.055	2.670	0.999
SOF_2	5.425	3.575	0.999
SO_2	7.095	2.472	0.999

In the PD signal detection system, the coupling capacitor (C_k) is used to extract the pulse current, and the non-inductive impedance (Z_m) is used to convert this pulse current into a pulse voltage, which is sent to the digital storage oscilloscope (DSO, WavePro 7100XL, Lecroy, New York, NY, USA, analogue band: 1 GHz, sampling rate: 20 GHz, memory depth: 48 MB). This research uses the PD calibration circuit recommended by IEC 60270:2000 to calibrate the PD magnitude [48], and the calibration curve obtained is shown in Figure 3.
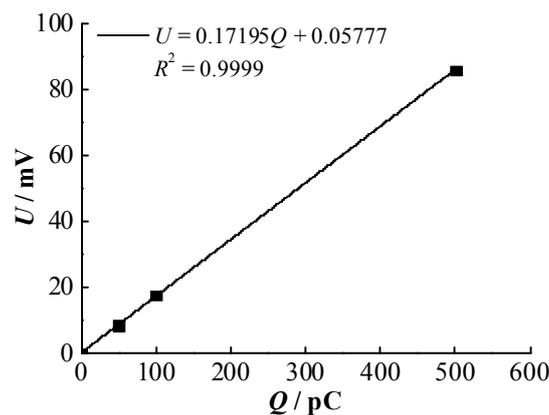
Figure 3. Calibration curve of PD magnitude.

2.2. Insulation Defect Model

Many types of insulation defects might occur in DC-GIE; however, the most common defect is free metal particles, which is metal powder that can move freely in a cavity. As shown in Figure 4, a ball-bowl electrode, which consists of a ball electrode, a bowl electrode, and 20 aluminum balls (mass fraction of C element: 0.88%), is developed to simulate the particle defect. The ball and bowl electrodes form a concentric sphere structure and are made of stainless steel (mass fraction of C element: 0.10%). The diameter of the ball electrode is 50 mm. A hollow sphere is cut to obtain the bowl electrode with a thickness of 1.5 mm. The diameters of the hollow sphere, circular incision, and aluminum ball are 100, 90, and 3 mm, respectively.
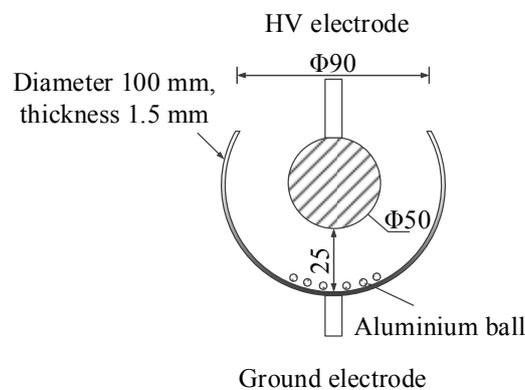

Figure 4. Insulation defect model (Unit: mm).

2.3. Experimental Method

All experiments are conducted under the same conditions: the laboratory temperature and relative humidity are maintained at 20 °C and 50%, respectively. The purity of new SF_6 gas is 99.9995%. The specific experimental steps are listed as follows:

(1) The experimental platform is connected as shown in Figure 1. The absolute alcohol is used to scrub the insulation defect model and the inner wall of the PD gas chamber. The chamber is set aside for 1 h to completely volatize the alcohol. The defect model is placed in the gas chamber.

(2) The PD gas chamber is vacuumed and then filled with 0.3 MPa new SF_6 gas. This process is repeated several times for purification. A GE600 mirror dew-point meter is used to measure the H_2O concentration, and a GPR-1200 ppm portable oxygen analyzer is used to measure the

O$_2$ concentration in the chamber. The concentrations of H$_2$O and O$_2$ are ensured to satisfy the industrial standard of DL/T 596-1996 [49].

(3) The voltage applied is gradually increased to the required experimental voltage. The decomposition experiment of SF$_6$ is conducted for 96 h under each voltage value. The SF$_6$ decomposed components are collected every 12 h. GC/MS is used to measure the concentrations of the decomposed components, and DSO is used to display and store the PD signals.

3. Experimental Results

3.1. PD Severity Division

The initial PD voltage U_g of the equipment without the particle defect is 82.2 kV. After placing the defect in the gas chamber, the initial PD voltage U_0 and breakdown voltage U_b of the equipment are 27.5 and 53.8 kV, respectively. The PD experiment is conducted under the grading voltage (Figure 5) to study the PD characteristics of the whole process when the applied voltage is increased. A total of 100 groups of PD signals are collected under each voltage value, and the PD parameters are obtained by averaging the three repeated experiments to ensure that the experimental results are statistically significant. Among the PD parameters, the discharge amplitude and repetition rate are two important features that can characterize the PD severity. The average discharge magnitude in a second (Q_{sec}, unit: pC/s) is selected as the characteristic quantity of PD severity to comprehensively consider the influence of these two parameters on PD development [26,27]. Q_{sec} is calculated using Equation (1).

$$Q_{sec} = Q_{avg} \times N \tag{1}$$

where Q_{avg} is the average charge of all single pulse within the measuring time (unit: pC/pulse) and N is the PD repetition rate (unit: pulse/s).
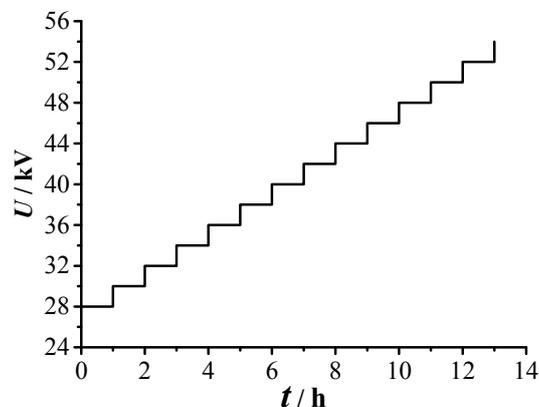

Figure 5. Experimental voltage and duration.

The change curves of three PD parameters with voltage applied are shown in Figure 6. With increasing experimental voltage, Q_{sec} gradually increases from about 3000 to 178,000 pC/s. This paper divides the PD into three levels according to Q_{sec} (region I: mild PD, region II: medium PD, and region III: dangerous PD) as shown in Table 2. When the applied voltage is slightly higher than the initial PD voltage (initial PD stage: from 28 to 30 kV), Q_{avg} and N grow rapidly. If the initial PD stage is excluded from region I, then the average growth rate of N in region II is the largest (reaching 35.58 pulse/(s·kV)), and the average growth rate of Q_{avg} in region III is the largest (reaching 9.99 pC/(pulse·kV)). Therefore, the division method for PD severity is reasonable.
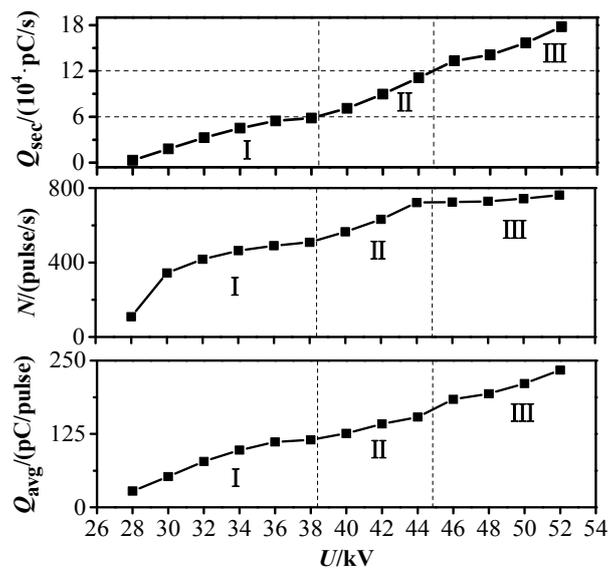
Figure 6. Three PD parameters over the applied voltage.

Table 2. Division of PD severity.

Q_{sec} (pC/s)	U/kV	Region	PD Severity
0–6×10^4	28, 30, 32, 34, 36, 38	I	Mild PD
6×10^4–12×10^4	40, 42, 44	II	Medium PD
12×10^4–18×10^4	46, 48, 50, 52	III	Dangerous PD

3.2. Analysis of SF$_6$ Decomposed Characteristics

Considering the limitations of the experimental conditions, two kinds of voltage in each abovementioned PD level are used for the decomposition experiment of SF$_6$. The total concentration of SF$_6$ decomposed components is small when the applied voltage is less than 30 kV. Therefore, six kinds of voltage (mild PD: 32, 36 kV; medium PD: 40, 44 kV; and dangerous PD: 48, 52 kV) are used for the experiments, and SF$_6$ decomposed characteristics are used to diagnose the PD severity. Experimental results show that five stable decomposed components, namely, CF$_4$, CO$_2$, SO$_2$F$_2$, SOF$_2$, and SO$_2$ are detected under each voltage value.

3.2.1. Formation Characteristics of Carbon-Containing Components

The formation process of SF$_6$ decomposed components is shown in Figure 7 [24]. CF$_4$ is generated through the reaction of C atom with F atom. Under the effect of the electric field, the charged particles hit the surface of the stainless-steel electrodes and aluminum balls to release the C atoms, as well as hit the SF$_6$ molecules and break six S-F bonds to generate F atoms; both processes require high-energy collision ionization. By calculation [50], the energy of the charged particle is low when the voltage $U \leq 36$ kV [26,27]. Therefore, when the voltage $U \leq 36$ kV, only a small amount of C atoms and F atoms are generated from the collision ionization, and the CF$_4$ concentration increases slowly with time (Figure 8a). When the voltage $U > 36$ kV, the energy of the charged particle increases. Thus, the growth rate of CF$_4$ concentration also increases. In particular, the CF$_4$ concentration quickly increases after 60 h. Limited F atoms are produced within 60 h. Thus, these limited F atoms have high possibility of reacting with metal and generate metal fluoride as compared with C atoms. This phenomenon limits the formation of CF$_4$ to some extent. After 60 h, the formed C atoms and F atoms continue to accumulate, and the excess F atoms will react with the C atoms and produce CF$_4$. Thus, the growth rate of CF$_4$ concentration accelerates.
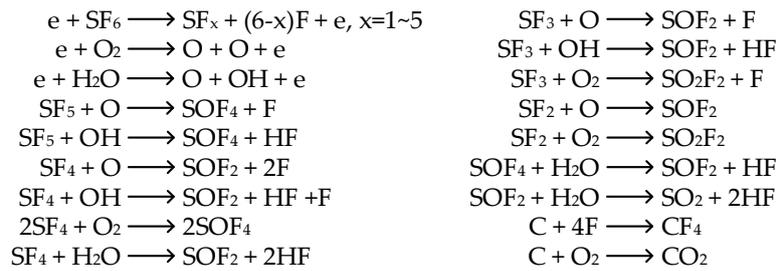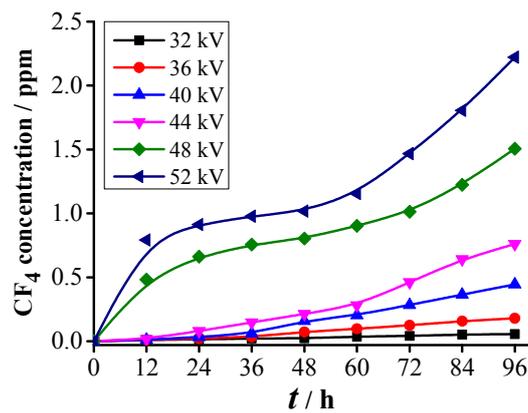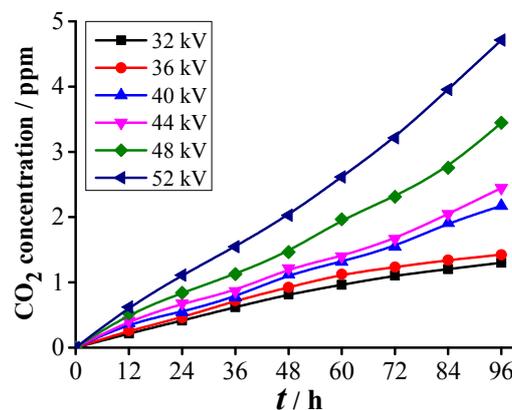
$$e + SF_6 \longrightarrow SF_x + (6-x)F + e, \ x=1\sim5 \qquad SF_3 + O \longrightarrow SOF_2 + F$$
$$e + O_2 \longrightarrow O + O + e \qquad SF_3 + OH \longrightarrow SOF_2 + HF$$
$$e + H_2O \longrightarrow O + OH + e \qquad SF_3 + O_2 \longrightarrow SO_2F_2 + F$$
$$SF_5 + O \longrightarrow SOF_4 + F \qquad SF_2 + O \longrightarrow SOF_2$$
$$SF_5 + OH \longrightarrow SOF_4 + HF \qquad SF_2 + O_2 \longrightarrow SO_2F_2$$
$$SF_4 + O \longrightarrow SOF_2 + 2F \qquad SOF_4 + H_2O \longrightarrow SOF_2 + HF$$
$$SF_4 + OH \longrightarrow SOF_2 + HF + F \qquad SOF_2 + H_2O \longrightarrow SO_2 + 2HF$$
$$2SF_4 + O_2 \longrightarrow 2SOF_4 \qquad C + 4F \longrightarrow CF_4$$
$$SF_4 + H_2O \longrightarrow SOF_2 + 2HF \qquad C + O_2 \longrightarrow CO_2$$

Figure 7. Formation process of SF_6 decomposed components.

The C atoms react with O_2 to generate CO_2. As shown in Figure 8b, the CO_2 concentration shows a saturated growth trend after 60 h when the voltage $U \leq 36$ kV. The C atoms in the surface of the stainless-steel electrodes and aluminum balls are gradually inspired with time, and only high-energy charged particles can inspire the C atoms in the deep layer. However, the energy of the charged particle at this stage is low, which inhibits the formation of CO_2. Thus, the CO_2 concentration presents a saturated growth trend. When the voltage $U > 36$ kV, the CO_2 concentration shows an approximately linear growth trend with time, which indicates that the charged particles at this stage can stimulate the deeper C atoms under the surface of the stainless-steel electrodes and aluminum balls.
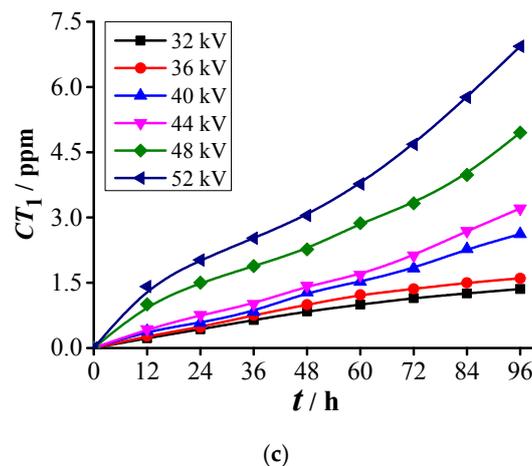

(**a**)

(**b**)

Figure 8. *Cont.*

(**c**)

Figure 8. Change of carbon-containing components with time: (**a**) CF_4; (**b**) CO_2; and (**c**) CT_1.

No organic insulating material exists near the PD area initiated by the particle defect. Thus, the concentration of (CF_4 + CO_2) can be used to characterize the amount of the carbon-containing metal involved in the reactions. CT_1 is defined to characterize the deterioration degree of carbon-containing metal in DC-GIE, and its formula is as follows:

$$CT_1 = C(CF_4) + C(CO_2) \tag{2}$$

where $C(CF_4)$ and $C(CO_2)$ represent the concentrations of CF_4 and CO_2 (unit: ppm), respectively. As shown in Figure 8c, when mild PD (32 and 36 kV) occurs, CT_1 shows a saturated growth trend at the end of the experiment. When medium PD (40 and 44 kV) occurs, CT_1 presents an approximately linear growth trend with time. When dangerous PD (48 and 52 kV) occurs, CT_1 shows an approximately "J" growth trend at the end of the experiment. The change curves of CT_1 differ under three different PD levels. Thus, CT_1 can be associated with the PD severity.

3.2.2. Formation Characteristics of Sulfur-Containing Components

SO_2F_2 is mainly produced through the reaction of SF_2 with O_2. The average O_2 concentration on the six experiments in the gas chamber is 1080 ppm. The sum of the concentration of the oxygen-containing components (CO_2, SO_2F_2, SOF_2, and SO_2) is less than 72 ppm, which indicates that O_2 is abundant in the formation of SO_2F_2. Thus, the formation characteristic of SO_2F_2 is mainly determined by the SF_2 concentration produced. Under the effect of the electric field, the charged particles hit the SF_6 molecules and break four S-F bonds to generate SF_2, which requires high-energy collision ionization [26,51]. The energy of the charged particle is not high when the voltage $U \leq 48$ kV (Figure 9a). Therefore, the amount of the produced SF_2 is small, and the SO_2F_2 concentration grows slowly within 24 h. However, the SF_2 formed continues to accumulate with time, and the SO_2F_2 concentration presents an approximately linear growth trend after 36 h. When the voltage increases to 52 kV, the SO_2F_2 concentration shows an approximately linear increase with time. However, when the experimental voltage $U \leq 52$ kV, with increasing voltage, the SO_2F_2 concentration remains less than 2 ppm, which illustrates that the SF_2 generated under the PD initiated by the particle defect can only produce a small amount of SO_2F_2.
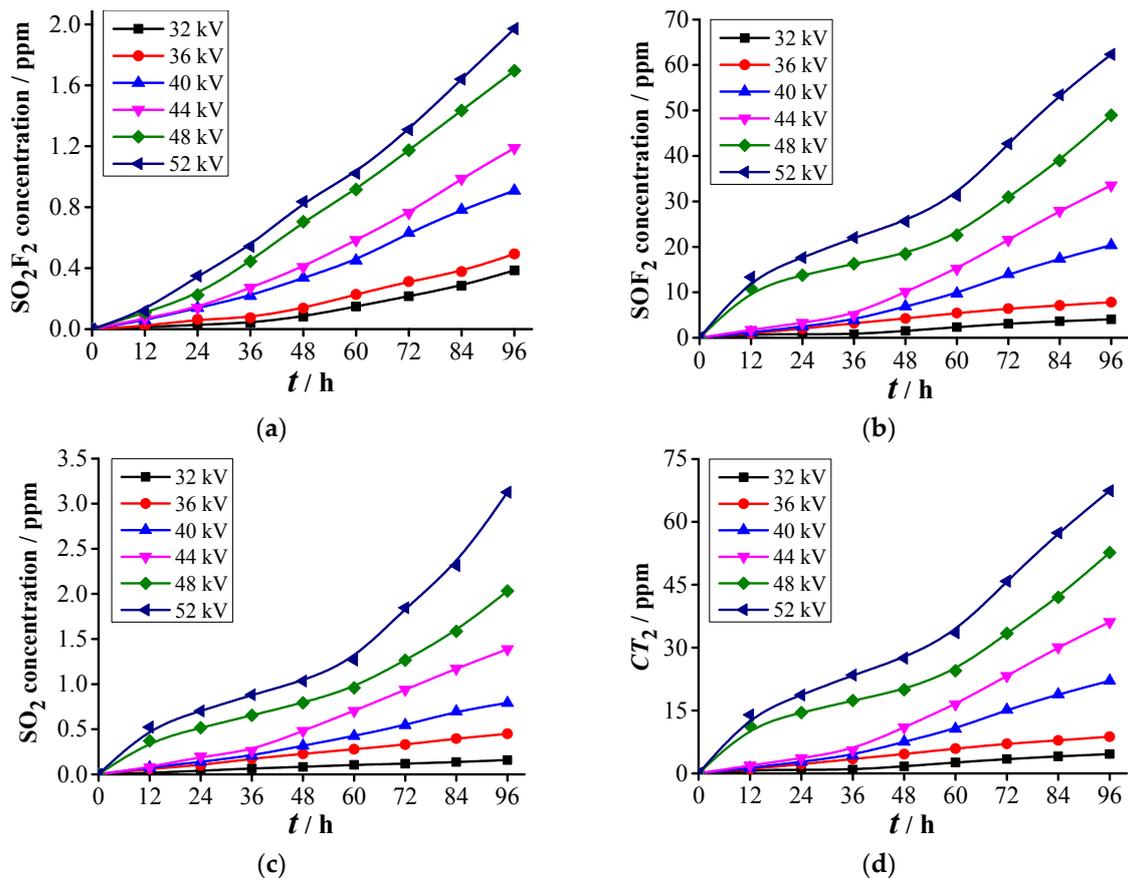
Figure 9. Change of sulfur-containing components with time: (**a**) SO_2F_2; (**b**) SOF_2; (**c**) SO_2; and (**d**) CT_2.

SOF_2 is mainly generated through the reaction of SF_4 with H_2O. In the early stage of the experiment ($t \leq 36$ h), when the voltage $U \leq 44$ kV, the formation of SF_4 is limited by the PD energy to some extent, thus the SOF_2 concentration increases slowly (Figure 9b). When the voltage $U > 44$ kV, the increase rate of SOF_2 concentration accelerates, however, the increase rate within 12 h $< t \leq 36$ h is lower than that within $t \leq 12$ h. Which can be explained by two points: (1) with the increase in the applied voltage, the collision ionizations intensify, thus the SF_4 concentration grows rapidly; (2) the H_2O near the PD area are gradually consumed with time, which inhibits the formation of SOF_2 when 12 h $< t \leq 36$ h. In the late stage of the experiment ($t \geq 60$ h), the SF_4 produced continues to accumulate, gradually spreads into the main gas chamber area, and reacts with the H_2O in this area. The average H_2O concentration of six experiments in the gas chamber is 313 ppm. The highest concentration of SOF_2 in Figure 9b is 62.3 ppm. The H_2O concentration is five times higher than the SOF_2 concentration, which can satisfy the requirement for generating SOF_2. Therefore, the growth rate of SOF_2 concentration accelerates, and the SOF_2 concentration shows an approximately linear increase with time.

As shown in Figure 9c, the growth trend of SO_2 concentration with time is similar to that of SOF_2 concentration under the same voltage. SOF_2 reacts with H_2O to generate SO_2 and HF. The SO_2 concentration at 96 h is 2.03 ppm under 52 kV, which is much lower than the H_2O concentration (313 ppm) in the gas chamber. Therefore, the formation characteristic of SO_2 is mainly determined by the produced SOF_2, as in, the growth trend of SO_2 concentration is similar to that of SOF_2 concentration.

The concentration of (SO_2F_2 + SOF_2 + SO_2) can roughly reflect the amount of SF_6 gas decomposed by the PD. Therefore, CT_2 is defined to characterize the deterioration degree of SF_6 gas-insulated medium in DC-GIE, and its formula is as follows:

$$CT_2 = C(SO_2F_2) + C(SOF_2) + C(SO_2) \tag{3}$$

where $C(SO_2F_2)$, $C(SOF_2)$, and $C(SO_2)$ represent the concentrations of SO_2F_2, SOF_2, and SO_2 (unit: ppm), respectively. As shown in Figure 9, the growth trend of CT_2 with time is similar to that of SOF_2 concentration under the same voltage. When the voltage applied is 52 kV, the SOF_2 concentration is nearly 30 times the SO_2F_2 concentration and 20 times the SO_2 concentration at 96 h. Thus, the change trend of CT_2 is mainly determined by the SOF_2 produced. The change curves of CT_2 are different under three different PD levels. Thus, CT_2 can be associated with the PD severity.

4. PD Severity Diagnosis

The concentration ratios of SF_6 decomposed components for the PD recognition in GIE are proposed according to the three-ratio method used in oil chromatographic analysis to eliminate the influence of the volume effect and time effect on the fault diagnosis [22–24]. These concentration ratios have definite physical meaning but are not necessarily the optimal feature subset for PD recognition. These ratios do not necessarily have the maximum relevance with the PD types and are possibly relevant with each other, which will introduce redundant information to the PD recognition. And the other concentration ratios might be advantageous for PD recognition. Furthermore, the features applicable to the PD type recognition are not necessarily suitable for the PD severity diagnosis. Therefore, this study selects the optimal feature subset for PD severity diagnosis based on the minimum-redundancy-maximum-relevance (mRMR) principle.

4.1. mRMR Principle

mRMR is a feature selection method based on the mutual information. In this method, the features are selected according to the maximum statistical dependency principle [28–33]; it finds m features as the optimal subset with the maximum relevance to the target category and minimum redundancy between each other from all features. Maximum relevance (max D) and minimum redundancy (min R) are defined as follows:

$$\max D(S,c), \; D = \frac{1}{|S|} \sum_{x_i \in S} I(x_i; c) \tag{4}$$

$$\min R(S), \; R = \frac{1}{|S|^2} \sum_{x_i, x_j \in S} I(x_i; x_j) \tag{5}$$

where S is the selected feature subset; $|S|$ is the number of features in S; $I(x_i; c)$ is the mutual information between the feature x_i and the category c; and $I(x_i; x_j)$ is the mutual information between the features x_i and x_j. Given two random continuous variables x and y, if their probability densities are $p(x)$ and $p(y)$, respectively, and their joint probability density is $p(x, y)$, then the mutual information between x and y is defined as follows:

$$I(x;y) = \iint p(x,y) \log \frac{p(x,y)}{p(x)p(y)} \mathrm{d}x \mathrm{d}y \tag{6}$$

When x and y are random discrete variables, Equation (6) can be written as follows:

$$I(x;y) = \sum_x \sum_y p(x,y) \log \frac{p(x,y)}{p(x)p(y)} \tag{7}$$

In summary, the mRMR-based feature selection algorithm has two principles: (1) the MID principle, which requires the largest value of D (the mutual information between the feature and the category) minus R (the mutual information between the features) as shown in Equation (8); and (2) the MIQ principle, which requires the largest value of D divided by R as shown in Equation (9).

$$\max \Phi_1(D, R), \ \Phi_1 = D - R \tag{8}$$

$$\max \Phi_2(D, R), \ \Phi_2 = D/R \tag{9}$$

The set of all features (the number is *n*) is assumed as S_n, and *m* features ($m < n$) are selected from S_n according to the mRMR principle, which form the subset of S_m. The set of the remaining features is $\{S_n - S_m\}$. In order to obtain the subset S_{m+1}, another feature must be selected from $\{S_n - S_m\}$ and combined with S_m to form S_{m+1}, which also meets mRMR principle. Therefore, the ($m + 1$)-th feature should satisfy Equation (10) or (11).

$$\max_{x_i \in \{S_n - S_m\}} \left[I(x_i; c) - \frac{1}{m} \sum_{x_j \in S_m} I(x_i; x_j) \right] \tag{10}$$

$$\max_{x_i \in \{S_n - S_m\}} \left[m I(x_i; c) / \sum_{x_j \in S_m} I(x_i; x_j) \right] \tag{11}$$

4.2. Feature Selection

The previous analysis showed close relationships between $C(CF_4)$, $C(CO_2)$, $C(SO_2F_2)$, $C(SOF_2)$, $C(SO_2)$, CT_1, CT_2, and PD severity. Therefore, the set of concentration ratios for the PD severity diagnosis is constructed and shown in Table 3, which also provides a corresponding label for each ratio to facilitate the subsequent analysis. The concentration ratios of SF_6 decomposed components are continuous variables. The probability density functions of these ratios must have been established to calculate the mutual information between the concentration ratios. However, no institution has conducted relevant statistical studies. Therefore, this study discretizes the concentration ratios [52].

Table 3. Concentration ratios for PD severity diagnosis and their corresponding labels.

Concentration Ratio	Label	Concentration Ratio	Label	Concentration Ratio	Label
$C(CF_4)/C(CO_2)$	1	$C(CO_2)/C(SOF_2)$	8	$C(SO_2F_2)/CT_2$	15
$C(CF_4)/C(SO_2F_2)$	2	$C(CO_2)/C(SO_2)$	9	$C(SOF_2)/C(SO_2)$	16
$C(CF_4)/C(SOF_2)$	3	$C(CO_2)/CT_1$	10	$C(SOF_2)/CT_1$	17
$C(CF_4)/C(SO_2)$	4	$C(CO_2)/CT_2$	11	$C(SOF_2)/CT_2$	18
$C(CF_4)/CT_1$	5	$C(SO_2F_2)/C(SOF_2)$	12	$C(SO_2)/CT_1$	19
$C(CF_4)/CT_2$	6	$C(SO_2F_2)/C(SO_2)$	13	$C(SO_2)/CT_2$	20
$C(CO_2)/C(SO_2F_2)$	7	$C(SO_2F_2)/CT_1$	14	CT_1/CT_2	21

x and *y* are assumed to be two concentration ratio vectors, and the number of the elements in *x* and *y* are both *N*. First, the elements in *x* are sorted in ascending order by value, and the value range of the elements in *x* is $[x_{\min}, x_{\max}]$. This range is subsequently divided into N_x subintervals on average. If the number of the elements in the *i*-th subinterval is $n_x(i)$, the probability of the elements in *x* falling within the *i*-th subinterval is $n_x(i)/N$. Similarly, the probability of the elements in *y* falling within the *j*-th subinterval is $n_y(j)/N$, where $n_y(j)$ is the number of the elements in *y* falling within the *j*-th subinterval. If the number of the elements in *x* falling within the *i*-th subinterval and the corresponding elements in *y* falling within the *j*-th subinterval is $n_{xy}(i, j)$, then the probability of that is $n_{xy}(i, j)/N$. Therefore, the mutual information between *x* and *y* can be written as follows:

$$I(x; y) = \sum_{i=1}^{N_x} \sum_{j=1}^{N_y} \frac{n_{xy}(i, j)}{N} \log \frac{N n_{xy}(i, j)}{n_x(i) n_y(j)} \tag{12}$$

where N_y is the number of the subintervals of vector *y*. If the value of $n_x(i)$, $n_y(j)$, or $n_{xy}(i, j)$ is zero, then the value of $\log \frac{N n_{xy}(i,j)}{n_x(i) n_y(j)}$ is also denoted as zero.

　　　If the concentration ratios of SF_6 decomposed components will be used to diagnose the PD severity in DC-GIE, then the influence of PD time on these ratios must be small. Even if insulation defects are found in DC-GIE, the concentrations of decomposed components are basically stabilized after a long run. Thus, the concentration ratios are unlikely to include large fluctuations with time. Similar to the first two ratios in Table 3, almost all of the 21 ratios in the table stabilize after 60 h (Figure 10). Therefore, the data of concentration ratios after 60 h are used to diagnose the PD severity.
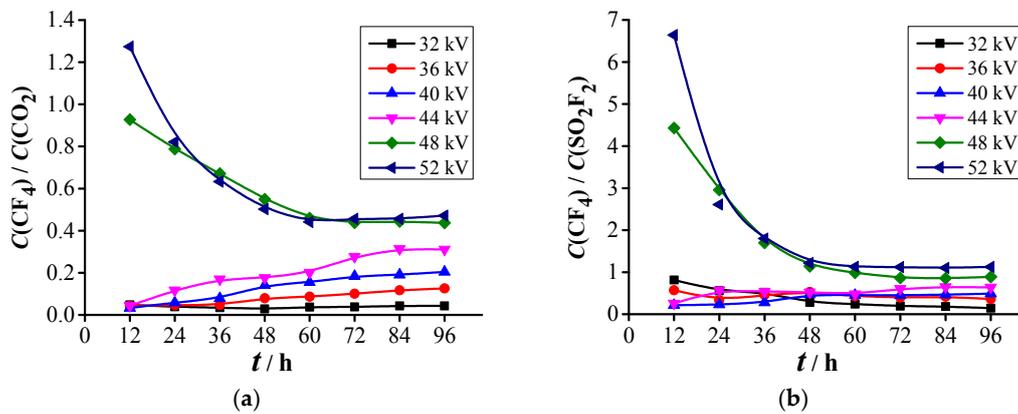

Figure 10. Change of concentration ratios with time: (**a**) $C(CF_4)/C(CO_2)$; and (**b**) $C(CF_4)/C(SO_2F_2)$.

　　　The feature sorting of the concentrations and concentration ratios of SF_6 decomposed components for the PD severity diagnosis is conducted based on the principles of MID and MIQ, respectively. The feature order is shown in Table 4, and the concentration ratios in the table are indicated by their corresponding labels. The first two features, namely, CF_4 and SOF_2, of the concentrations are the same, and the first four features, namely, $C(CO_2)/CT_1$, $C(CF_4)/C(SO_2)$, $C(CO_2)/C(SOF_2)$, and $C(CF_4)/C(CO_2)$, of the concentration ratios are also the same.

Table 4. Feature order based on mRMR principle.

Feature Order	mRMR Principle	
	MID	**MIQ**
Concentration order	CF_4, SOF_2, CO_2, SO_2, CT_2, SO_2F_2, CT_1	CF_4, SOF_2, SO_2, CT_2, CT_1, SO_2F_2, CO_2
Concentration ratio order	10, 4, 8, 1, 12, 5, 14, 2, 9, 3, 18, 7, 6, 11, 15, 16, 19, 21, 17, 20, 13	10, 4, 8, 1, 5, 12, 2, 3, 18, 14, 9, 6, 7, 11, 17, 15, 19, 21, 20, 16, 13

4.3. PD Severity Diagnosis

　　　The back propagation neural network (BPNN) [24,34–41] and support vector machine (SVM) [41–47] algorithms are used to diagnose the PD severity. The concentrations and concentration ratios of SF_6 decomposed components are selected as the input data, and three PD levels (mild PD, medium PD, and dangerous PD) are the output results. The total samples are randomly divided into six equal parts, five of which are used as the training samples, and the remaining one is used as the test sample. The diagnosis results are shown in Figure 11, and the prediction accuracy is the average value of 100 diagnoses. The prediction accuracy of PD severity obtained by using the concentration ratios is higher than that obtained by using the concentrations, and the prediction accuracy obtained by using SVM is higher than that obtained by using BPNN. Therefore, the concentration ratios are more suitable than the concentrations as the feature quantities for PD severity diagnosis. The SVM algorithm is complex; when the number of features is large, the computational complexity is huge. When the concentration ratios are used to diagnose the PD severity, the prediction accuracy obtained by using BPNN is also high, and the computational complexity of which is moderate. Therefore, we can select a suitable algorithm to diagnose the PD severity according to the actual situation.
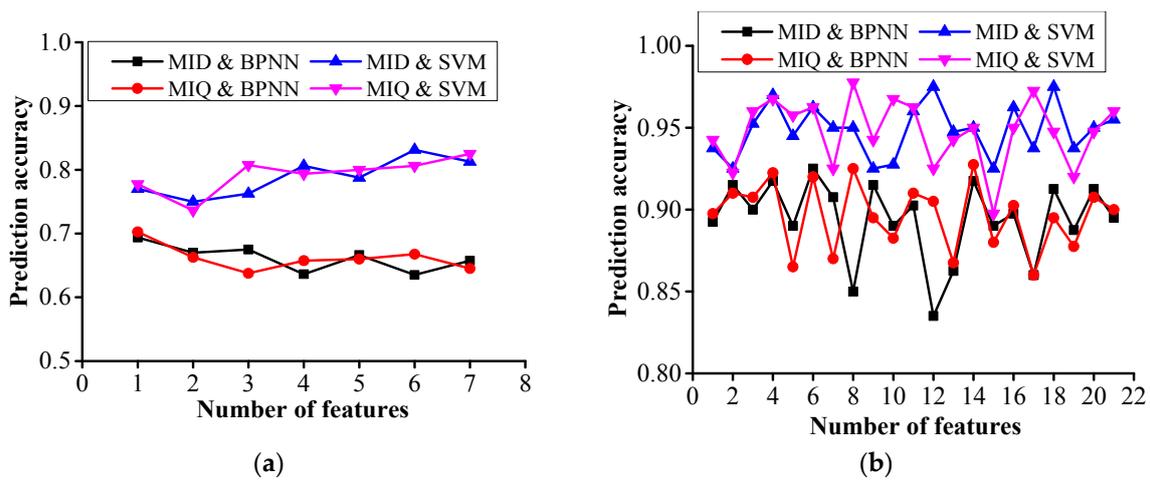
Figure 11. Predication accuracy over the number of features: (**a**) concentration feature; and (**b**) concentration ratio feature.

From the previous analysis, the first four concentration ratios, namely, $C(CO_2)/CT_1$, $C(CF_4)/C(SO_2)$, $C(CO_2)/C(SOF_2)$, and $C(CF_4)/C(CO_2)$, obtained by using the MID- and MIQ-based feature selection algorithms, are the same. Table 5 shows the highest three prediction accuracies and their corresponding numbers of features of each curve in Figure 11b. When using these four concentration ratios to diagnose the PD severity, the prediction accuracy obtained is on the top three, and the difference from the highest accuracy does not exceed 1%. Therefore, this research recommends using $C(CO_2)/CT_1$, $C(CF_4)/C(SO_2)$, $C(CO_2)/C(SOF_2)$, and $C(CF_4)/C(CO_2)$ to diagnose the PD severity initiated by a free metal particle defect in DC-GIE.

Twenty-four groups of concentration ratios in this paper are used as the training samples, and another set of experimental data is used as the test sample to verify the diagnosis performance of PD severity by using the abovementioned four concentration ratios. The concentration ratios in the test sample are obtained under the same experimental conditions as in this paper, and the deviations of the concentrations of SF_6 decomposed components between these two experiments are less than 10%. BPNN and SVM algorithms are used to diagnose the PD severity, and the confusion matrices of the diagnosis results are shown in Tables 6 and 7. The prediction accuracy of PD severity by using BPNN algorithm is: (7 + 7 + 8)/24 = 91.67%, and that obtained by using SVM algorithm is: (8 + 7 + 8)/24 = 95.83%, which both obtain good diagnosis effects.

Table 5. The highest three prediction accuracies and their corresponding concentration ratios.

mRMR Principle	Algorithm	Accuracy Order	Accuracy	Number of Features	Concentration Ratio Labels
MID	BPNN	1	92.5%	6	10, 4, 8, 1, 12, 5
		2	91.75%	4/14	10, 4, 8, 1/10, 4, 8, 1, 12, 5, 14, 2, 9, 3, 18, 7, 6, 11
		3	-	-	-
	SVM	1	97%	12/18	10, 4, 8, 1, 12, 5, 14, 2, 9, 3, 18, 7/10, 4, 8, 1, 12, 5, 14, 2, 9, 3, 18, 7, 6, 11, 15, 16, 19, 21
		2	-	-	-
		3	97.5%	4	10, 4, 8, 1
MIQ	BPNN	1	92.75%	14	10, 4, 8, 1, 5, 12, 2, 3, 18, 14, 9, 6, 7, 11
		2	92.5%	8	10, 4, 8, 1, 5, 12, 2, 3
		3	92.25%	4	10, 4, 8, 1
	SVM	1	97.75%	8	10, 4, 8, 1, 5, 12, 2, 3
		2	97.25%	17	10, 4, 8, 1, 5, 12, 2, 3, 18, 14, 9, 6, 7, 11, 17, 15, 19
		3	96.75%	4/10	10, 4, 8, 1/10, 4, 8, 1, 5, 12, 2, 3, 18, 14

Table 6. Confusion matrix of the diagnosis result based on the back propagation neural network (BPNN).

Real PD Severity	Number of Samples in Each PD Level in the Diagnosis Result		
	Mild PD	Medium PD	Dangerous PD
Mild PD	7	1	0
Medium PD	0	7	1
Dangerous PD	0	0	8

Table 7. Confusion matrix of the diagnosis result based on the support vector machine (SVM).

Real PD Severity	Number of Samples in Each PD Level in the Diagnosis Result		
	Mild PD	Medium PD	Dangerous PD
Mild PD	8	0	0
Medium PD	0	7	1
Dangerous PD	0	0	8

5. Discussion

The decomposition characteristics of SF_6 under different negative DC voltages are studied. The mRMR principle is used for the feature selection for PD severity diagnosis, and the BPNN and SVM algorithms are used to diagnose the PD severity. This research lays the foundation for the use of DCA method to diagnose the insulation faults in DC-GIE and to assess its insulation status. However, due to the limitations of the experimental conditions, only two kinds of voltage in each PD level are selected for the decomposition experiment of SF_6. More experiments should be performed in the future. H_2O, O_2, absorbent, and gas pressure in DC-GIE will affect the decomposition characteristics of SF_6; however, these factors are not considered in this study and thus require further research. In addition, more field data of SF_6 decomposed components should be obtained to verify and improve the performance of the proposed method in diagnosing PD severity.

6. Conclusions

- The PD characteristics of the whole process from the initial PD to the breakdown initiated by free metal particle defect in DC-GIE are studied. The average discharge magnitude in a second Q_{sec} is proposed to be used to characterize the PD severity. Based on Q_{sec}, the PD is divided into three levels: mild PD, medium PD, and dangerous PD.
- Two kinds of voltage in each abovementioned PD level are selected for the decomposition experiment of SF_6. Experimental results show that five stable decomposed components, namely, CF_4, CO_2, SO_2F_2, SOF_2, and SO_2, are detected under each voltage. The PD severity has close relationships with $C(CF_4)$, $C(CO_2)$, $C(SO_2F_2)$, $C(SOF_2)$, $C(SO_2)$, CT_1, and CT_2. The concentrations and concentration ratios of SF_6 decomposed components can be used to diagnose the PD severity.
- mRMR-based feature selection algorithm is used to sort the concentrations and concentration ratios of SF_6 decomposed components, and BPNN and SVM algorithms are used to diagnose the PD severity. The prediction accuracy of PD severity obtained by using the concentration ratios is higher than that obtained by using the concentrations, and the use of $C(CO_2)/CT_1$, $C(CF_4)/C(SO_2)$, $C(CO_2)/C(SOF_2)$, and $C(CF_4)/C(CO_2)$ shows good performance in diagnosing the PD severity.

Author Contributions: Ju Tang and Fuping Zeng conceived and designed the experiments; Xu Yang, Dong Yang, Qiang Yao, and Yulong Miao performed the experiments; Xu Yang, Chaohai Zhang and Fuping Zeng analyzed the data; Ju Tang and Xu Yang wrote the paper.

Conflicts of Interest: The authors declare no conflict of interest.

References

1. Benato, R.; Dughiero, F.; Forzan, M.; Paolucci, A. Proximity effect and magnetic field calculation in GIL and in isolated phase bus ducts. *IEEE Trans. Magn.* **2002**, *38*, 781–784. [CrossRef]
2. Benato, R.; Mario, C.D.; Koch, H. High-capability applications of long gas-insulated lines in structures. *IEEE Trans. Power Del.* **2007**, *22*, 619–626. [CrossRef]
3. Benato, R.; Brunello, P.; Fellin, L. Thermal behavior of EHV gas-insulated lines in Brenner pass pilot tunnel. *IEEE Trans. Power Del.* **2010**, *25*, 2717–2725. [CrossRef]
4. Benato, R.; Dughiero, F. Solution of coupled electromagnetic and thermal problems in gas-insulated transmission lines. *IEEE Trans. Magn.* **2003**, *39*, 1741–1744. [CrossRef]
5. Benato, R.; Napolitano, D. Reliability assessment of EHV gas-insulated transmission lines: Effect of redundancies. *IEEE Trans. Power Del.* **2008**, *23*, 2174–2181. [CrossRef]
6. Tenzer, M.; Koch, H.; Imamovic, D. Underground transmission lines for high power AC and DC transmission. In Proceedings of the 2016 IEEE/PES Transmission and Distribution Conference and Exposition, Dallas, TX, USA, 3–5 May 2016.
7. Magier, T.; Tenzer, M.; Koch, H. Direct current gas-insulated transmission lines. *IEEE Trans. Power Del.* **2017**. [CrossRef]
8. Mendik, M.; Lowder, S.M.; Elliott, F. Long term performance verification of high voltage DC GIS. In Proceedings of the 1999 IEEE Transmission and Distribution Conference, New Orleans, LA, USA, 11–16 April 1999; pp. 484–488.
9. Ohki, Y. Thyristor valves and GIS in Kii channel HVDC link. *IEEE Electr. Insul. Mag.* **2001**, *17*, 78–79. [CrossRef]
10. Hasegawa, T.; Yamaji, K.; Hatano, M. Development of insulation structure and enhancement of insulation reliability of 500 kV DC GIS. *IEEE Trans. Power Del.* **1997**, *12*, 192–202. [CrossRef]
11. Hasegawa, T.; Yamaji, K.; Hatano, M. DC dielectric characteristics and conception of insulation design for DC GIS. *IEEE Trans. Power Del.* **1996**, *11*, 1776–1782. [CrossRef]
12. Beyer, C.; Jenett, H.; Kfockow, D. Influence of reactive SF_x gases on electrode surfaces after electrical discharges under SF_6 atmosphere. *IEEE Trans. Dielectr. Electr. Insul.* **2000**, *7*, 234–240. [CrossRef]
13. Chu, F.Y. SF_6 decomposition in gas-insulated equipment. *IEEE Trans. Dielectr. Electr. Insul.* **1986**, *21*, 693–725. [CrossRef]
14. Van Brunt, R.J.; Herron, J.T. Fundamental processes of SF_6 decomposition and oxidation in glow and corona discharges. *IEEE Trans. Dielectr. Electr. Insul.* **1990**, *25*, 75–94. [CrossRef]
15. Chang, C.; Chang, C.S.; Jin, J.; Hoshino, T.; Hanai, M.; Kobayashi, N. Source classification of partial discharge for gas insulated substation using wave shape pattern recognition. *IEEE Trans. Dielectr. Electr. Insul.* **2005**, *12*, 374–386. [CrossRef]
16. Dreisbusch, K.; Kranz, H.G.; Schnettler, A. Determination of a failure probability prognosis based on PD-diagnostics in GIS. *IEEE Trans. Dielectr. Electr. Insul.* **2008**, *15*, 1707–1714. [CrossRef]
17. Istad, M.; Runde, M. Thirty-six years of service experience with a national population of gas-insulated substations. *IEEE Trans. Power Del.* **2010**, *25*, 2448–2454. [CrossRef]
18. Van Brunt, R.J. Production rates for oxy-fluorides SOF_2, SO_2F_2 and SOF_4 in SF_6 corona discharges. *J. Res. Natl. Bur. Stand.* **1985**, *90*, 229–253. [CrossRef]
19. Piemontesi, M.; Niemeyer, L. Sorption of SF_6 and SF_6 decomposition products by activated alumina and molecular sieve 13X. In Proceedings of the 1996 IEEE International Symposium on Electrical Insulation, Montreal, QC, Canada, 16–19 June 1996; pp. 828–838.
20. Van Brunt, R.J.; Herron, J.T. Plasma chemical model for decomposition of SF_6 in a negative glow corona discharge. *Phys. Scr.* **1994**, *53*, 9–29. [CrossRef]
21. Prakash, K.S.; Srivastava, K.D.; Morcos, M.M. Movement of particles in compressed SF_6 GIS with dielectric coated enclosure. *IEEE Trans. Dielectr. Electr. Insul.* **1997**, *4*, 344–347. [CrossRef]
22. Tang, J.; Liu, F.; Zhang, X.X.; Meng, Q.H.; Zhou, J.B. Partial discharge recognition through an analysis of SF_6 decomposition products part 1: Decomposition characteristics of SF_6 under four different partial discharges. *IEEE Trans. Dielectr. Electr. Insul.* **2012**, *19*, 29–36. [CrossRef]

23. Tang, J.; Liu, F.; Meng, Q.H.; Zhang, X.X.; Tao, J.G. Partial discharge recognition through an analysis of SF$_6$ decomposition products part 2: Feature extraction and decision tree-based pattern recognition. *IEEE Trans. Dielectr. Electr. Insul.* **2012**, *19*, 37–44. [CrossRef]

24. Tang, J.; Yang, X.; Ye, G.X.; Yao, Q.; Miao, Y.L.; Zeng, F.P. Decomposition characteristics of SF$_6$ and partial discharge recognition under negative DC conditions. *Energies* **2017**, *10*, 556. [CrossRef]

25. Majidi, M.; Oskuoee, M. Improving pattern recognition accuracy of partial discharges by new data preprocessing methods. *Electr. Power Syst. Res.* **2015**, *119*, 100–110. [CrossRef]

26. Tang, J.; Zeng, F.P.; Pan, J.Y.; Zhang, X.X.; Yao, Q. Correlation analysis between formation process of SF$_6$ decomposed components and partial discharge qualities. *IEEE Trans. Dielectr. Electr. Insul.* **2013**, *20*, 864–875. [CrossRef]

27. Tang, J.; Pan, J.Y.; Zhang, X.X.; Zeng, F.P.; Yao, Q.; Hou, X.Z. Correlation analysis between SF$_6$ decomposed components and charge magnitude of partial discharges initiated by free metal particles. *IET Sci. Meas. Technol.* **2014**, *8*, 170–177. [CrossRef]

28. Ashkezari, A.D.; Ma, H.; Saha, T.K.; Cui, Y. Investigation of feature selection techniques for improving efficiency of power transformer condition assessment. *IEEE Trans. Dielectr. Electr. Insul.* **2014**, *21*, 836–844. [CrossRef]

29. Peng, H.C.; Long, F.H.; Ding, C. Feature selection based on mutual information: Criteria of max-dependency, max-relevance, and min-redundancy. *IEEE Trans. Pattern Anal. Mach. Intell.* **2005**, *27*, 1226–1238. [CrossRef] [PubMed]

30. Li, Y.B.; Yang, Y.T.; Li, G.Y. A fault diagnosis scheme for planetary gearboxes using modified multi-scale symbolic dynamic entropy and mRMR feature selection. *Mech. Syst. Signal. Pr.* **2017**, *91*, 295–312. [CrossRef]

31. Escalona-Vargas, D.; Siegel, E.R.; Murphy, P.; Lowery, C.L.; Eswaran, H. Selection of reference channels based on mutual information for frequency-dependent subtraction method applied to fetal biomagnetic signals. *IEEE Trans. Biomed. Eng.* **2017**, *64*, 1115–1122. [CrossRef] [PubMed]

32. Xu, Y.; Ding, Y.X.; Ding, J.; Wu, L.Y.; Xue, Y. Mal-Lys: Prediction of lysine malonylation sites in proteins integrated sequence-based features with mRMR feature selection. *Sci. Rep.* **2016**, *6*, 38318. [CrossRef] [PubMed]

33. Ramirez-Gallego, S.; Lastra, I.; Martinez-Rego, D.; Bolon-Canedo, V.; Benitez, J.M.; Herrera, F.; Alonso-Betanzos, A. Fast-mRMR: Fast minimum redundancy maximum relevance algorithm for high-dimensional big data. *Int. J. Intell. Syst.* **2017**, *32*, 134–152. [CrossRef]

34. Aminian, M.; Aminian, F. Neural-network based analog-circuit fault diagnosis using wavelet transform as preprocessor. *IEEE Trans. Circuits Syst. II Analog Digit. Signal Process.* **2000**, *47*, 151–156. [CrossRef]

35. Karnin, E.D. A simple procedure for punning back-propagation trained neural networks. *IEEE Trans. Neural Netw.* **1990**, *1*, 239–242. [CrossRef] [PubMed]

36. Mas'ud, A.A.; Albarracín, R.; Ardila-Rey, J.A.; Muhammad-Sukki, F.; Illias, H.A.; Bani, N.A.; Munir, A.B. Artificial neural network application for partial discharge recognition: Survey and future directions. *Energies* **2016**, *9*, 574–591. [CrossRef]

37. Majidi, M.; Fadali, M.S.; Etezadi-Amoli, M.; Oskuoee, M. Partial discharge pattern recognition via sparse representation and ANN. *IEEE Trans. Dielectr. Electr. Insul.* **2015**, *22*, 1061–1070. [CrossRef]

38. Gulski, E.; Krivda, A. Neural networks as a tool for recognition of partial discharges. *IEEE Trans. Dielectr. Electr. Insul.* **1993**, *28*, 984–1001. [CrossRef]

39. Satish, L.; Zaengl, W.S. Artificial neural networks for recognition of 3-D partial discharge patterns. *IEEE Trans. Dielectr. Electr. Insul.* **1994**, *1*, 265–275. [CrossRef]

40. Hozumi, N.; Okamoto, T.; Imajo, T. Discrimination of partial discharge patterns using a neural network. *IEEE Trans. Dielectr. Electr. Insul.* **1992**, *27*, 550–556. [CrossRef]

41. Leng, X.Z.; Wang, J.H.; Ji, H.B.; Wang, Q.G.; Li, H.M.; Qian, X.; Li, F.Y.; Yang, M. Prediction of size-fractionated airborne particle-bound metals using MLR, BP-ANN and SVM analyses. *Chemosphere* **2017**, *180*, 513–522. [CrossRef] [PubMed]

42. Tang, J.; Zhuo, R.; Wang, D.B.; Wu, J.R.; Zhang, X.X. Application of SA-SVM incremental algorithm in GIS PD pattern recognition. *J. Electr. Eng. Technol.* **2016**, *11*, 192–199. [CrossRef]

43. Tang, J.; Tao, J.G.; Zhang, X.X.; Liu, F. Multiple SVM-RFE for feature subset selection in partial discharge pattern recognition. *Int. Rev. Electr. Eng. I.* **2012**, *7*, 5240–5246.

44. Tang, J.; Wang, D.B.; Fan, L.; Zhuo, R.; Zhang, X.X. Feature parameters extraction of GIS partial discharge signal with multifractal detrended fluctuation analysis. *IEEE Trans. Dielectr. Electr. Insul.* **2015**, *22*, 3037–3045. [CrossRef]

45. Naseri, F.; Jafari, F.; Mohseni, E.; Tang, W.C.; Feizbakhsh, A.; Khatibinia, M. Experimental observations and SVM-based prediction of properties of polypropylene fibres reinforced self-compacting composites incorporating nano-CuO. *Coustr. Build. Mater.* **2017**, *143*, 589–598. [CrossRef]

46. Wei, Q.; Wu, B.; Xu, D.W.; Zargari, N.R. Natural sampling SVM-based common-mode voltage reduction in medium-voltage current source rectifier. *IEEE Trans. Power Electr.* **2017**, *32*, 7553–7560. [CrossRef]

47. Gonzalez-Costa, J.J.; Reigosa, M.J.; Matias, J.M.; Covelo, E.F. Soil Cd, Cr, Cu, Ni, Pb and Zn sorption and retention models using SVM: Variable selection and competitive model. *Sci. Total Environ.* **2017**, *593*, 508–522. [CrossRef] [PubMed]

48. IEC 60270:2000 High-voltage Test Techniques—Partial Discharge Measurements. Available online: http://www.doc88.com/p-868119919771.html (accessed on 20 June 2017).

49. DL/T 596–1996 Preventive Test Code for Electric Power Equipment. Available online: http://www.doc88.com/p-9763610841190.html (accessed on 20 June 2017).

50. Zhou, W.J.; Zheng, Y.; Yang, S.; Li, H.; Wang, B.S.; Qiao, S.Y. Detection of intense partial discharge of epoxy insulation in SF_6 insulated equipment using carbonyl sulfide. *IEEE Trans. Dielectr. Electr. Insul.* **2016**, *23*, 2942–2948. [CrossRef]

51. Tang, J.; Zeng, F.P.; Zhang, X.X.; Pan, J.Y.; Yao, Q.; Hou, X.Z.; Tang, Y. Relationship between decomposition gas ratios and partial discharge energy in GIS, and the influence of residual water and oxygen. *IEEE Trans. Dielectr. Electr. Insul.* **2014**, *21*, 1226–1234. [CrossRef]

52. Kraskov, A.; Stögbauer, H.; Grassberger, P. Estimating mutual information. *Phys. Rev. E Stat. Nonlin. Soft Matter Phys.* **2004**, *69*, 066138. [CrossRef] [PubMed]